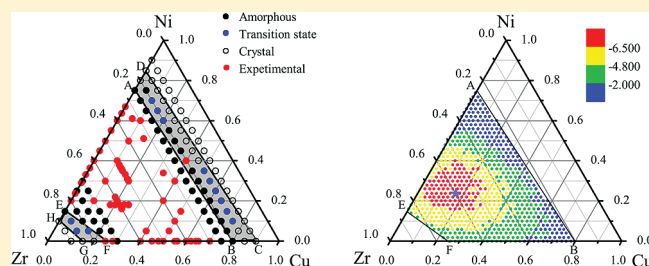


# Prediction of Favored and Optimized Compositions for Cu–Zr–Ni Metallic Glasses by Interatomic Potential

Y. Y. Cui, J. H. Li, Y. Dai, and B. X. Liu\*

Advanced Materials Laboratory, Department of Materials Science and Engineering, Tsinghua University, Beijing 100084, China

**ABSTRACT:** For the Cu–Zr–Ni system, an interatomic potential was constructed under the newly proposed formalism named smoothed and long-range second-moment approximation of tight-binding. Applying the constructed potential, molecular dynamics simulations were carried out to compare the relative stability of crystalline solid solution versus its disordered counterpart. Simulations not only reveal that the origin of metallic glass formation is the crystalline lattice collapsing while the solute concentrations exceed critical values, but also determine a quadrilateral region, within which the metallic glass formation is energetically favored. Moreover, the energy differences between the crystalline solid solutions and the disordered states were considered as the driving force for amorphization and were computed by molecular static calculations. The calculation results located an optimized composition area with the driving force much greater than those outside. In addition, the alloys around the composition of  $\text{Cu}_{16}\text{Zr}_{60}\text{Ni}_{24}$  were identified to have maximum driving force, and the atomic configurations were also analyzed by the Voronoi tessellation method.



## I. INTRODUCTION

Since the first finding of millimeter-diameter glassy rods in the Pd–Cu–Si system,<sup>1</sup> bulk metallic glasses (BMGs) with excellent glass-forming ability have been developed in many multicomponent alloy systems and have exhibited inviting properties, such as high yield strength, hardness, elastic strain limit, and corrosion resistance.<sup>2–4</sup> It is commonly thought that BMGs formation in multicomponent alloys is primarily attributed to the chemical complexity of these systems.<sup>5,6</sup> The empirical rules for the prediction of element selection and glass formation range were framed by Johnson<sup>5</sup> and Inoue et al.<sup>6</sup> as follows: (1) multicomponent alloys with three or more elements, (2) more than 12% atomic radius difference between elements, (3) negative heat of mixing between main elements, and (4) the deep eutectic rule resulting from the reduced glass transition criterion. Although these rules have served as guidelines for the synthesis of BMGs in the past decade, they still belong to the empirical approaches, and predicted compositions for metallic glass formation were not satisfactory enough. In the authors' view, it is a good choice to study glass formation compositions of a metal system from its interatomic potential because if a realistic interatomic potential of a metallic system is constructed, the interactions between the atoms are known, and then most of the chemical and physical properties, including the glass formation compositions, can be determined through relevant computations or simulations.<sup>7,8</sup>

As a candidate for BMGs, the Cu–Zr–Ni system has been extensively studied because of its excellent glass-forming ability and good mechanical properties.<sup>9–13</sup> For instance, Zhang et al. first found that the  $\text{Cu}_{20}\text{Zr}_{60}\text{Ni}_{20}$  amorphous alloys exhibited a wide

supercooled liquid region of 60 K by liquid melt quenching technology.<sup>9</sup> Yang et al. obtained the Cu–Zr–Ni glassy rods with the diameter of 1 mm by copper mold casting within the composition range of 56–64 at. % Zr, 16–26 at. % Cu, and 16–24 at. % Ni.<sup>10</sup> Hu et al. reported that the amorphous  $\text{Cu}_{10}\text{Zr}_{90-x}\text{Ni}_x$  ( $x = 20–60$ ) and  $\text{Cu}_{40}\text{Zr}_{60-x}\text{Ni}_x$  ( $x = 5–40$ ) alloys were synthesized by mechanical alloying methods.<sup>11</sup> From the thermodynamic point of view, several studies have calculated the glass forming compositions of the Cu–Zr–Ni system on the basis of Miedema's model and Alonso's method, suggesting that the Cu–Zr–Ni system is a readily glass-forming system.<sup>14,15</sup> The findings from both experimental and theoretical aspects triggered our interest to study the glass forming ability of the Cu–Zr–Ni system at an atomic level through the interatomic simulations.

In the present study, we would address three issues: (i) A smoothed and long-range second-moment approximation of tight binding (TB-SMA) potential was first constructed for the Cu–Zr–Ni system. (ii) On the basis of the constructed Cu–Zr–Ni potential, a series of molecular dynamics (MD) simulations were then conducted to identify the composition region within which the metallic glass formation is favored. (iii) In the determined composition region, a scheme of molecular statics (MS) calculations were carried out to pinpoint the optimized compositions, and Voronoi tessellation analysis was employed to study the atomic configurations of the alloy around the optimized composition.

Received: January 4, 2011

Revised: March 22, 2011

Published: April 07, 2011

## II. CONSTRUCTION OF CU–ZR–NI INTERATOMIC POTENTIAL

The atomic configurations of the Cu–Zr–Ni system are governed by the interatomic potential. If the interatomic potential of the system is known, most of the chemical and physical properties, as well as the glass-forming compositions, can be determined.<sup>7,8</sup> In this section, we attempt to construct an interatomic potential for the Cu–Zr–Ni system under the newly proposed smoothed and long-range second-moment approximation of tight binding (TB-SMA).<sup>16,17</sup>

The expression of the TB-SMA interatomic potential can be written as follows:

$$E_i = \sum_{j \neq i} \phi(r_{ij}) - \sqrt{\sum_{j \neq i} \psi(r_{ij})} \quad (3)$$

$$\phi(r_{ij}) = \begin{cases} A_1 \exp \left[ -p_1 \left( \frac{r_{ij}}{r_0} - 1 \right) \right] & r_{ij} \leq r_{m1} \\ A_{1m} \exp \left[ -p_{1m} \left( \frac{r_{ij}}{r_0} - 1 \right) \right] \left( \frac{r_{c1}}{r_0} - \frac{r_{ij}}{r_0} \right)^{n1} & r_{m1} < r_{ij} \leq r_{c1} \end{cases} \quad (4)$$

$$\psi(r_{ij}) = \begin{cases} A_2 \exp \left[ -p_2 \left( \frac{r_{ij}}{r_0} - 1 \right) \right] & r_{ij} \leq r_{m2} \\ A_{2m} \exp \left[ -p_{2m} \left( \frac{r_{ij}}{r_0} - 1 \right) \right] \left( \frac{r_{c2}}{r_0} - \frac{r_{ij}}{r_0} \right)^{n2} & r_{m2} < r_{ij} \leq r_{c2} \end{cases} \quad (5)$$

where  $E_i$  is the total potential energy of atom  $i$  and  $r_{ij}$  is the distance between atoms  $i$  and  $j$  of the system at equilibrium;  $r_{m1}$  and  $r_{m2}$  are the transition points of the pair item and the density item;  $r_{c1}$  and  $r_{c2}$  are the cutoff radii of the pair item and the density item; and  $A_1$ ,  $p_1$ ,  $A_{1m}$ ,  $p_{1m}$ ,  $A_2$ ,  $p_2$ ,  $A_{2m}$ , and  $p_{2m}$  are potential parameters. From eqs 4 and 5, one can see that the pair and density terms, as well as their high derivatives, can continuously and smoothly go to zero at the cutoff radii  $r_{c1}$  and  $r_{c2}$ , thus removing the jumps of energy and force, avoiding some nonphysical behaviors in the simulations.<sup>18</sup>

For the Cu–Zr–Ni system, there should be six sets of potential parameters; (i.e. three sets for Cu–Cu, Zr–Zr and Ni–Ni) and three sets for Cu–Zr, Zr–Ni and Cu–Ni. The potential parameters of Cu–Cu, Zr–Zr, and Ni–Ni were determined by fitting to their physical properties obtained by experiments.<sup>19,20</sup> The Cu–Zr, Zr–Ni and Cu–Ni cross-potentials were constructed by fitting to the physical properties of the intermetallic compounds. For the Cu–Zr intermetallic compounds, the property data were adopted from Ghosh's paper.<sup>21</sup> Because there were few data available for the Zr–Ni and Cu–Ni intermetallic compounds, ab initio calculations were conducted to identify the structures of several Zr–Ni and Cu–Ni intermetallic compounds and obtain their physical properties. The ab initio calculations were carried out using the Cambridge serial total energy package code of Materials Studio.<sup>22</sup> In the calculations, the nonlocal ultrasoft pseudopotentials were adopted to describe the electron–ion interaction, which allowed the use of a moderate energy cutoff for the construction of the plane-wave basis for the transition metals.<sup>7</sup>

The exchange and correlation items were described by the generalized-gradient approximation of Perdew and Wang, and the precision of the calculations was set at the ultrafine class.<sup>22</sup> There were 10–35  $k$ -points generated in the first Brillouin zone,

**Table 1. Parameters of the Constructed Potential of Cu–Zr–Ni System**

	Cu	Zr	Ni	Cu–Zr	Zr–Ni	Cu–Ni
$p_1$	9.625 372	8.202 755	11.087 57	7.701 745	6.285 048	9.787 880
$A_1$ (eV)	0.315 491	0.751 605	0.287 580	0.607 641	0.863 621	0.287 804
$r_{m1}$ (Å)	2.124 148	3.355 556	1.976 092	2.444 527	2.661 513	1.961 680
$n_1$	4	4	4	4	4	4
$p_{1m}$	2.860 823	2.110 120	4.485 833	1.585 780	0.003 995	3.348 093
$A_{1m}$ (eV)	8.049 825	3.104 994	8.372 519	8.445 146	8.020 719	8.099 770
$r_{c1}$ (Å)	3.634 148	5.466 890	3.486 092	4.331 234	4.479 059	3.528 742
$p_2$	4.903 930	4.817 954	3.669 412	4.551 226	3.772 868	4.820 816
$A_2$ (eV <sup>2</sup> )	3.854 734	16.924 785	4.991 288	10.646 367	20.728 02	4.215 374
$r_{m2}$ (Å)	3.611 361	3.218 719	2.803 510	2.390 458	1.777 376	3.583 014
$n_2$	5	5	5	5	5	5
$p_{2m}$	0.000 602	0.000 198	0.000 695	0.000 478	0.000 321	0.000 601
$A_{2m}$ (eV <sup>2</sup> )	0.458 708	13.997 855	0.671 240	14.501 495	21.035 31	0.463 089
$r_{c2}$ (Å)	6.215 324	6.556 265	6.200 000	5.560 000	5.560 000	6.200 000
$r_0$ (Å)	2.553 618	3.215 897	2.492 155	2.884 757	2.854 026	2.522 886

**Table 2. Lattice Constants ( $a$  and  $c$ ), Cohesive Energies ( $E_c$ ), Elastic Constants ( $C_{ij}$ ) and Bulk Moduli ( $B_0$ ) of Cu, Zr, and Ni Fitted to the Potential and the Experimental Data<sup>a</sup>**

	fcc-Cu		hcp-Zr		fcc-Ni	
	fitted	exptl	fitted	exptl	fitted	exptl
$a$ (Å)	3.611	3.615	3.219	3.232	3.524	3.517
$c$ (Å)			5.249	5.147		
$E_c$ (eV)	3.502	3.490	6.258	6.250	4.423	4.440
$C_{11}$ (Mbar)	1.688	1.683	1.415	1.434	2.385	2.418
$C_{12}$ (Mbar)	1.225	1.221	0.772	0.728	1.630	1.550
$C_{13}$ (Mbar)			0.666	0.653		
$C_{33}$ (Mbar)			1.544	1.648		
$C_{44}$ (Mbar)	0.745	0.757	0.208	0.320	1.217	1.242
$B_0$ (Mbar)	1.361	1.370	0.956	0.833	1.882	1.860

<sup>a</sup> The data in the left column for each element are fitted to the tight-binding potentials, and those in the right column are the experimental data.<sup>19,20</sup>

which varied from structure to structure.<sup>17</sup> The geometry optimization was first performed to determine the lattice constants and the total energies of the Zr–Ni and Cu–Ni intermetallic compounds, and then the bulk modulus was calculated. The formation energies of the Zr–Ni and Cu–Ni intermetallic compounds can be easily derived from the total energies.

In summary, the potential parameters for the Cu–Zr–Ni system are listed in Table 1. To testify to the relevance of the potential, the reproduced data are listed in Table 2 and Table 3, showing that the reproduced properties match well with the experimental properties. The constructed Cu–Zr–Ni potential was then used to carry out a series of interatomic simulations in the next two sections

## III. EVALUATION OF GLASS-FORMING REGION

The process of producing the metallic glasses is always a nonequilibrium or even far-from-equilibrium process, and the related kinetic condition is quite restricted.<sup>2,4</sup> Taking the liquid melt quenching technique as an example, a cooling speed higher than

**Table 3.** Lattice Constants (*a*, *b*, and *c*), Formation Energies (*E<sub>f</sub>*), and Bulk Moduli (*B<sub>0</sub>*) of the Cu–Zr, Ni–Zr, and Ni–Cu Compounds Reproduced from the Potential and the Results from Ab Initio Calculations<sup>a</sup>

	compd									
	Cu <sub>5</sub> Zr	Cu <sub>8</sub> Zr <sub>3</sub>	Cu <sub>10</sub> Zr <sub>7</sub>	CuZr <sub>2</sub>	Ni <sub>3</sub> Zr	NiZr	NiZr <sub>3</sub>	Ni <sub>3</sub> Cu	NiCu	NiCu <sub>3</sub>
space group	<i>F</i> $\bar{4}3m$	<i>Pnma</i>	<i>Aba2</i>	<i>I4/mmm</i>	<i>Pm</i> $\bar{3}$ <i>m</i>	<i>Pm</i> $\bar{3}$ <i>m</i>	<i>Pm</i> $\bar{3}$ <i>m</i>	<i>Pm</i> $\bar{3}$ <i>m</i>	<i>Pm</i> $\bar{3}$ <i>m</i>	<i>Pm</i> $\bar{3}$ <i>m</i>
<i>a</i> or <i>a</i> , <i>c</i> or <i>a</i> , <i>b</i> , <i>c</i> (Å)	6.92	7.88,8.15,10.16	9.37,9.39,12.78	3.24,11.20	3.699	3.179	4.344	3.557	2.778	3.547
	6.87	7.87,8.15, 9.98	9.34,9.32,12.67	3.22,11.18	3.760	3.211	4.280	3.554	2.806	3.607
<i>E<sub>c</sub></i> (eV)	4.079	4.432	4.821	5.481	5.392	5.783	5.839	4.192	3.907	3.728
	4.080	4.431	4.820	5.481	5.403	5.777	5.840	4.191	3.980	3.727
<i>B<sub>0</sub></i> (Mbar)	1.286	1.268	1.162	1.126	1.441	1.025	1.053	1.716	1.514	1.539
	1.392			1.121	1.658	1.040	0.984	1.839	1.656	1.535

<sup>a</sup> The data in the first line are reproduced from the tight-binding potential, and those in the second line are the results from ab initio calculations.<sup>22</sup>

10<sup>6</sup> K/s is frequently required to avoid crystallization of any possible crystalline phase.<sup>2</sup> Such a high cooling speed makes the kinetic condition rather restricted, and therefore, the intermetallic phases, which frequently have complicated structures, could hardly nucleate or grow. It follows that the phase competing against the amorphous phase is the solid solution with one of three simple structures: fcc, bcc, or hcp. This viewpoint has been supported by a large number of research results from both experimental and theoretical aspects.<sup>15,23</sup> Consequently, the issue related to predicting the glass forming region of the Cu–Zr–Ni system in our study could be converted into an issue of comparing the relative stability of the solid solution versus its amorphous counterpart.

The constructed Cu–Zr–Ni potential was then used to carry out a series of MD simulations using the solid solution models.<sup>7</sup> The stable crystalline structures of Cu, Zr, and Ni at the simulation temperature (300 K) are fcc, hcp, and fcc, respectively;<sup>24</sup> therefore, two types of solid solution models—the fcc and hcp—were used. The fcc solid solution model consists of 9 × 9 × 9 = 2916 atoms and the hcp solid solution model consists of 13 × 8 × 7 × 4 = 2912 atoms. For both fcc and hcp solid solution models, the [100] and [001] crystalline directions are parallel to the *x* and *z* axes, respectively, and the crystalline directions along the *y* axis are [010] for fcc and [120] for hcp. In setting the solid solution models, the solute atoms were added by random substitution of a certain number of solvent atoms to obtain a desired concentration. The periodic boundary conditions were adopted in three directions. The MD simulations were carried out with the Parrinello–Rahman constant pressure scheme at zero pressure and 300 K.<sup>25</sup> The motion equations were solved using a second-order, four-value predictor corrector algorithm with a time step *t* = 5 × 10<sup>−15</sup> s.<sup>26</sup> The structural changes were monitored by the projection of atomic positions, which can visually reflect the state of the system, and the pair-correlation function *g*(*r*), which is commonly used to identify an amorphous phase.<sup>7</sup>

We now present the simulation results of the Cu–Zr–Ni system. After adequate MD time, the Cu–Zr–Ni models reach a relatively stable state; that is, the energy of the system and the atomic configurations are almost unchanged. Assume that *E<sub>am</sub>* is the energy per atom of the Cu<sub>*x*</sub>Zr<sub>*y*</sub>Ni<sub>1−*x−y*</sub> amorphous phase and *E<sub>Cu</sub>*, *E<sub>Zr</sub>*, and *E<sub>Ni</sub>* are the experimental lattice energies of Cu, Zr, and Ni respectively.<sup>19,20</sup> The formation enthalpy for the amorphous phase Δ*H<sup>am</sup>* can thus be expressed by

$$\Delta H^{\text{am}} = E_{\text{am}} - [xE_{\text{Cu}} + yE_{\text{Zr}} + (1 - x - y)E_{\text{Ni}}] \quad (6)$$

Inspecting the results of MD simulations, the structures of the Cu–Zr–Ni models exhibit three different states: a crystal state,

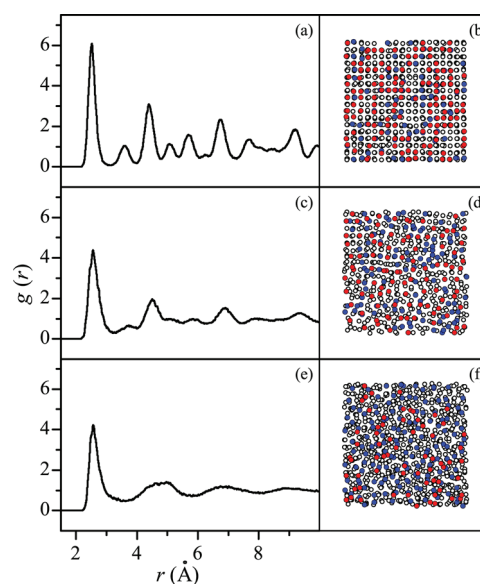


**Figure 1.** The projections of atomic positions and total pair-correlation functions, *g*(*r*), for (a, b) the crystal state (Cu<sub>30</sub>Zr<sub>10</sub>Ni<sub>60</sub>), (c, d) the transition state (Cu<sub>20</sub>Zr<sub>20</sub>Ni<sub>60</sub>), and (e, f) the amorphous state (Cu<sub>10</sub>Zr<sub>30</sub>Ni<sub>60</sub>). Blue solid circle is for Zr, open circle is for Ni, and red solid circle is for Cu.

an ordered–disordered coexisting state, and an amorphous state. We take three compositions—Cu<sub>30</sub>Zr<sub>10</sub>Ni<sub>60</sub>, Cu<sub>20</sub>Zr<sub>20</sub>Ni<sub>60</sub>, and Cu<sub>10</sub>Zr<sub>30</sub>Ni<sub>60</sub>—as examples. Figure 1 shows the pair-correlation function, *g*(*r*), and projections of atomic positions for the three states. From the figure, one sees that the *g*(*r*) curves of the Cu<sub>30</sub>Zr<sub>10</sub>Ni<sub>60</sub> feature apparent crystal peaks in Figure 1a, exhibiting a long-range ordered feature. For the *g*(*r*) curves of the Cu<sub>20</sub>Zr<sub>20</sub>Ni<sub>60</sub>, some crystal peaks have disappeared, whereas others still remain (Figure 1c), exhibiting an order–disorder coexisting feature. For the *g*(*r*) curves of Cu<sub>10</sub>Zr<sub>30</sub>Ni<sub>60</sub>, the crystal peaks beyond the second peak have disappeared in Figure 1e, exhibiting a short-range ordered and long-range disordered feature. Further inspecting Figure 1, one can see that the projections of the atomic positions of Cu<sub>30</sub>Zr<sub>10</sub>Ni<sub>60</sub> show a completely ordered state, and those of Cu<sub>10</sub>Zr<sub>30</sub>Ni<sub>60</sub> show a completely disordered state. For the Cu<sub>20</sub>Zr<sub>20</sub>Ni<sub>60</sub>, the locally ordered regions coexist with locally disordered regions, exhibiting an ordered–disordered coexisting state. To verify this ordered–disordered coexisting state, we have conducted the MD simulations of Cu<sub>20</sub>Zr<sub>20</sub>Ni<sub>60</sub> (order–disorder coexisting



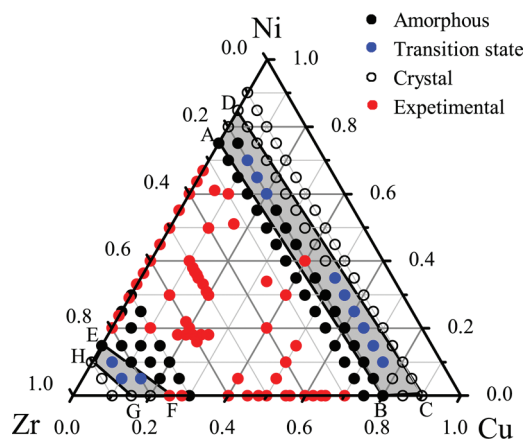


**Figure 2.** The glass-forming composition diagram derived from MD simulations for the Cu–Zr–Ni ternary system.

state) solid solution model with a larger simulation box with  $10 \times 10 \times 4 = 4000$  atoms for a longer time of 3 000 000 time steps to reach a relatively stable state, in which the energy drift was  $<10^{-3}$  eV/atom per million steps. After adequate MD simulation time steps, we still found the locally ordered region coexisting with the locally disordered region in the simulation cell.

According to the pair-correlation function  $g(r)$  and projections of atomic positions, we split the Cu–Zr–Ni composition triangle into five regions by four critical solubility lines and constructed the glass-forming composition diagram in Figure 2. One can see from Figure 2 that when an alloy composition is located beyond line HG and moving toward the Zr corner, or beyond line CD and moving toward the Cu–Ni side, the crystalline structures can remain stable. These regions were consequently classified as the crystal regions. When the composition of the alloy moves from the line AB and line EF toward the central quadrilateral region, enclosed by ABFE, the crystalline structure becomes unstable and would collapse, turning into a disordered state. This quadrilateral region was defined as the amorphous region. Between the crystal regions and the amorphous region, there are ordered–disordered coexisting state regions, within which the initial solid solutions would transform into a state featuring an ordered–disordered coexisting structure.

From the above description, a glass-forming composition diagram with a quadrilateral composition region favoring metallic glass formation was determined in Figure 2. For the binary Cu–Ni alloys, the equilibrium phase diagram shows that Cu and Ni are completely miscible and could form a fcc solid solution in the entire composition range,<sup>24</sup> implying it is difficult to obtain amorphous alloys along the Cu–Ni side, which is in accordance with the crystal region in Figure 2. To validate the amorphous region in Figure 2, experimental results were collected and marked by red solid circles in the figure.<sup>9–13,27–33</sup> These experimentally measured glass-formation compositions mostly fall within the quadrilateral region, suggesting that the results predicted by MD simulations are acceptable in determining the glass-forming ability of the Cu–Zr–Ni system.

#### IV. OPTIMIZATION OF GLASS-FORMING COMPOSITIONS

On the basis of the constructed interatomic potential, the glass-forming composition diagram has been figured out in the previous section, from which one may conveniently predict the

possibility of the Cu–Zr–Ni metallic glasses' forming at a given composition. However, there is still an open issue whether we can pinpoint the optimized composition in the amorphous region. From a thermodynamics viewpoint, the formation enthalpy difference between the amorphous phase and the solid solution could serve as the driving force of amorphization.<sup>7</sup> The formation enthalpy of amorphous phase  $\Delta H^{\text{am}}$  has been calculated through the MD results in the previous section. For solid solutions, there may be some difficulties in calculating the formation enthalpy through MD simulations because when the composition falls in the amorphous region of the composition diagram, the solid solution models in MD simulations are unstable, and they would spontaneously turn into the amorphous state.

Recently, an efficient and relevant scheme to predict the formation enthalpy of the ternary metal systems through molecular statics (MS) calculations has been proposed by Dai et al., and the predicted results matched well with those obtained by experiments or ab initio calculations.<sup>34</sup> The MS calculations were also carried out on the basis of the interatomic potential and conducted in the solid solution models as those in the MD simulations. However, The MS calculations differ from the MD simulations in the following three aspects: First, the objective of the MD simulations was to give the information concerning the process of the crystal-to-amorphous transition as well as to reveal the mechanism of the metallic glass formation, whereas the objective of MS calculations was to optimize the solid solution models and find the minimum energies in the solid solution models at a certain composition. Second, by comparing the relative stability of crystalline solid solution and its disordered counterpart during the MD simulations, the solid solution models may collapse when the solute concentrations exceed critical values, whereas during the MS calculations, the lattice constants were set to vary with a slight interval, yet keeping the solid solution models remaining in crystal structures. Third, in the MD simulations, the motion equations were solved using a second-order, four-value predictor corrector algorithm within a certain time step, whereas in the MS calculations, the forces on the atoms were not calculated so that the motion equations did not need to be solved.

In this section, MS calculations were carried out on the basis of the constructed interatomic potential to calculate the formation enthalpy of Cu–Zr–Ni solid solution. The simulation models were first set up in the same way as in MD simulations, and then MS calculations were carried out to optimize the solid solutions so as to find the minimum energies at different compositions. During energy optimization, the lattice constant was allowed to vary with a small interval of 0.001 Å, yet keeping the model in the crystal structure. Assuming that  $E_{\text{min}}$  is the minimum energy per atom of the  $\text{Cu}_x\text{Zr}_y\text{Ni}_{1-x-y}$  solid solutions and  $E_{\text{Cu}}$ ,  $E_{\text{Zr}}$ , and  $E_{\text{Ni}}$  are the experimental lattice energies of Cu, Zr, and Ni, respectively, the formation enthalpy for  $\text{Cu}_x\text{Zr}_y\text{Ni}_{1-x-y}$  solid solutions  $\Delta H^{\text{s.s}}$  can be expressed by

$$\Delta H^{\text{s.s}} = E_{\text{min}} - [xE_{\text{Cu}} + yE_{\text{Zr}} + (1 - x - y)E_{\text{Ni}}] \quad (7)$$

The formation enthalpy difference between the amorphous phase and the solid solution thus can be written as

$$\Delta H^{\text{am} - \text{s.s}} = \Delta H^{\text{am}} - \Delta H^{\text{s.s}} \quad (8)$$

where  $\Delta H^{\text{am} - \text{s.s}}$  serves as the driving force of amorphization.

We now discuss the calculated results of the Cu–Zr–Ni systems. On the basis of the results from MD simulations and MS calculations, the color mapping of the amorphization driving force was plotted in Figure 3. One can see from the figure that the

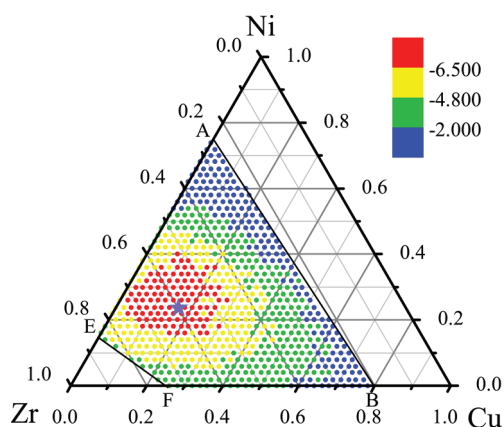


**Figure 3.** The formation enthalpy difference between the amorphous phase and the solid solution calculated from MS simulations.

$\Delta H^{\text{am-s.s.}}$  is negative over the whole amorphous region, suggesting that the formation enthalpy of the amorphous phase is lower than that of the solid solution so that the formation of the amorphous phase is energetically favored. Further inspecting the figure, one can find that the compositions marked by red dots have a lower  $\Delta H^{\text{am-s.s.}}$  than any other regions, and within the red dots region, the  $\text{Cu}_{16}\text{Zr}_{60}\text{Ni}_{24}$  composition marked by a purple pentagon has the lowest  $\Delta H^{\text{am-s.s.}}$ . As mentioned above, the larger the formation enthalpy difference, the stronger the driving force of amorphization; therefore, the optimized compositions for metallic glass formation can be pinpointed around  $\text{Cu}_{16}\text{Zr}_{60}\text{Ni}_{24}$ .

It is interesting and important to compare the present results with those reported by experiments. The collected experimental data in Figure 2 were densely distributed around the optimized composition region, suggesting that the alloys around the optimized region were readily obtained.<sup>9–11</sup> Yang et al. have obtained a series of glassy rods at the composition of  $\text{Cu}_{40-x}\text{Zr}_{60}\text{Ni}_x$  ( $x = 14, 16, 18, 20, 22, 24, 26$ ) and  $\text{Cu}_x\text{Zr}_{82-x}\text{Ni}_{18}$  ( $x = 14, 18, 20, 22, 24, 26, 30$ ), finding the alloy  $\text{Cu}_{20}\text{Zr}_{62}\text{Ni}_{18}$  has the largest reduced glass-transition temperature.<sup>10</sup> Hu et al. also found the large supercooled liquid region is 34 K for  $\text{Cu}_{10}\text{Zr}_{60}\text{Ni}_{30}$  and 48 K for  $\text{Cu}_{20}\text{Zr}_{60}\text{Ni}_{20}$ .<sup>11</sup> The results obtained from interatomic simulations are consistent with that from experiments. From a physical point of view, the predicted amorphous region and optimized composition are calculated from the realistic Cu–Zr–Ni potential, which governs the atomic configurations and, thus, in turn, governs the energetic states of both solid solution and the amorphous phase of the Cu–Zr–Ni system. The simulation results are supported by the experimental observations, thus providing additional evidence to the relevance of the constructed Cu–Zr–Ni potential.

## V. VORONOI TESSELLATION ANALYSIS OF OPTIMIZED COMPOSITION

After pinpointing the optimized composition of the Cu–Zr–Ni metallic glasses, it is of interest to further deduce the atomic configurations of the alloy around the optimized composition. In this section, the atomic configurations were analyzed by the Voronoi tessellation method, which is often employed to characterize the local atomic structure of metallic glasses.<sup>35–37</sup> In the Voronoi tessellations, the Voronoi polyhedrons around Cu, Zr, and Ni atoms were analyzed independently. Some small cell faces—say, smaller than 5% of the average face

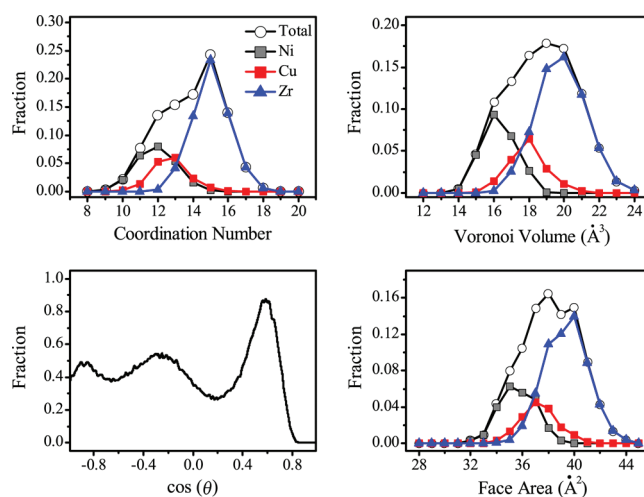


**Figure 4.** The coordination number distribution, the Voronoi cell volume, the cosine of bond angle distributions, and the face area for the amorphous  $\text{Cu}_{16}\text{Zr}_{60}\text{Ni}_{24}$ .

area of the cell—were neglected in counting the CN in the analyses. By doing so, the degeneracy problem and the effects of thermal vibration could be minimized.<sup>38</sup>

After Voronoi tessellation analysis, the coordination number (CN) distribution, the Voronoi cell volume, the cosine distribution of bond angle, and the face area of the amorphous  $\text{Cu}_{16}\text{Zr}_{60}\text{Ni}_{24}$  were calculated, and the results are presented in Figure 4. It can be seen from Figure 4a that the dominating coordination polyhedrons of the  $\text{Cu}_{16}\text{Zr}_{60}\text{Ni}_{24}$  metallic glasses are icosihexahedron (CN = 15). Inspecting the partial coordination polyhedrons, we see the dominating polyhedrons of Zr are icosihexahedron (CN = 15), those of Ni are icosahedron (CN = 12), and those of Cu are icosidihedron (CN = 13). In the Voronoi analysis, the CNs of the atoms in both the ideal fcc and hcp structures are 12.<sup>35</sup> The Goldschmidt atomic radii of Zr, Ni, and Cu are 1.47, 1.25, and 1.28 Å, respectively.<sup>24</sup> Because Zr is a hcp metal that has larger atomic radii than Ni and Cu, the predominant short-range local packing unit of Zr should have more than 12 coordination atoms with the adding of Ni and Cu, which is, indeed, observed in the Voronoi analysis. Meanwhile, the average cell volume and the average face area of Zr are larger than those of Ni and those of Cu. The results are also consistent with the atomic radii of Zr (1.47 Å), Ni (1.25 Å), and Cu (1.28 Å).<sup>24</sup>

## VI. CONCLUDING REMARKS

We have shown that for the Cu–Zr–Ni system, on the basis of a realistic interatomic potential, molecular dynamics simulations not only revealed the origin of the metallic glass formation but also quantitatively determined a quadrilateral region in the composition triangle, within which the metallic glass formation is energetically favored. Moreover, molecular statics calculations were conducted to identify an optimized composition region, within which the driving force for producing the Cu–Zr–Ni metallic glasses reaches its maximum value, suggesting that the alloys with the overall compositions designed around the optimized composition of  $\text{Cu}_{16}\text{Zr}_{60}\text{Ni}_{24}$  could be the most obtainable.

## AUTHOR INFORMATION

### Corresponding Author

\*dmslxb@tsinghua.edu.cn.

## ■ ACKNOWLEDGMENT

The authors are grateful for financial support from the National Natural Science Foundation of China (50871058 and 50971072), the Ministry of Science and Technology of China (2011CB606301), the Ministry of Education of China (200800030054), and the Administration of Tsinghua University.

## ■ REFERENCES

- (1) Chen, H. S. *Acta Metal.* **1974**, *22*, 1505–1511.
- (2) Wang, W. H.; Dong, C.; Shek, C. H. *Mater. Sci. Eng., R* **2004**, *44*, 45–89.
- (3) Wang, L. M.; Tian, Y. J.; Liu, R. P.; Richert, R. J. *Phys. Chem. B* **2010**, *114*, 3618–3622.
- (4) Schroers, J. *Adv. Mater.* **2010**, *22*, 1566–1597.
- (5) Johnson, W. L. *MRS Bull.* **1999**, *24*, 42–56.
- (6) Inoue, A.; Takeuchi, A. *Mater. Trans.* **2002**, *43*, 1892–1906.
- (7) Li, J. H.; Dai, X. D.; Liang, S. H.; Tai, K. P.; Kong, Y.; Liu, B. X. *Phys. Rep.* **2008**, *455*, 1–134.
- (8) Liang, S. H.; Dai, Y.; Li, J. H.; Liu, B. X. *J. Phys. Chem. B* **2010**, *114*, 9540–9545.
- (9) Zhang, T.; Inoue, A.; Masumoto, T. *Mater. Sci. Eng., A* **1994**, *182*, 1423–1426.
- (10) Yang, H.; Wang, J. Q.; Li, Y. J. *Non-Cryst. Solids* **2006**, *352*, 832–836.
- (11) Hu, C. J.; Lee, P. Y. *Mater. Chem. Phys.* **2002**, *74*, 13–18.
- (12) Ming, M.; Altounian, Z. *J. Non-Cryst. Solids* **1996**, *205*, 633–636.
- (13) Peto, G.; Bakonyi, L.; Tompa, K.; Guzzi, L. *Phys. Rev. B* **1995**, *52*, 7151–7158.
- (14) Wang, T. L.; Li, J. H.; Liu, B. X. *Phys. Chem. Chem. Phys.* **2009**, *11*, 2371–2373.
- (15) Basu, J.; Murty, B. S.; Ranganathan, S. J. *Alloys Compd.* **2008**, *465*, 163–172.
- (16) Rosato, V.; Guillope, M.; Legrand, B. *Philos. Mag. A* **1989**, *59*, 321–336.
- (17) Li, J. H.; Dai, X. D.; Wang, T. L.; Liu, B. X. *J. Phys.: Condens. Matter* **2007**, *19*, 086228.
- (18) Frenkel, D.; Smit, B. *Understanding Molecular Simulation: from Algorithms to Applications*; Academic: New York, 2002.
- (19) Kittel, C. *Introduction to solid state physics*; Wiley: New York, 2002.
- (20) Lide, D. R. *CRC Handbook of Chemistry and Physics*; CRC Press: New York, 2007.
- (21) Ghosh, G. *Acta Mater.* **2007**, *55*, 3347–3374.
- (22) Segall, M. D.; Lindan, P.; Probert, M. J.; Pickard, C. J.; Hasnip, P. J.; Clark, S. J.; Payne, M. C. *J. Phys.: Condens. Matter* **2002**, *14*, 2717–2744.
- (23) Dai, Y.; Li, J. H.; Che, X. L.; Liu, B. X. *J. Phys. Chem. B* **2009**, *113*, 7282–7290.
- (24) Massalski, T. B.; Okamoto, H.; Subramanian, P. R.; Kacprzak, L. *Binary Alloy Phase Diagrams*; ASM International: Materials Park, OH, 1990.
- (25) Parrinello, M.; Rahman, A. *J. Appl. Phys.* **1981**, *52*, 7182–7190.
- (26) Allen, M. P.; Tildesley, D. J. *Computer Simulation of Liquids*; Clarendon: Oxford, 1981.
- (27) Garaguly, J.; Lovas, A.; Tompa, K.; Takacs, J. J. *Alloys Compd.* **1997**, *253*, 114–117.
- (28) Ristic, R.; Stubicar, M.; Babic, E. *Philos. Mag.* **2007**, *87*, 5629–5637.
- (29) Stojanova, L.; Russew, K. *Mater. Sci. Eng., A* **1997**, *226*, 483–486.
- (30) Wang, H. R.; Gao, Y. L.; Hui, X. D.; Min, G. H.; Chen, Y.; Ye, Y. F. *J. Alloys Compd.* **2003**, *349*, 129–133.
- (31) Buschow, K. H. J. *J. Appl. Phys.* **1981**, *52*, 3319–3323.
- (32) Altounian, Z.; Stromolsen, J. O. *Phys. Rev. B* **1983**, *27*, 4149–4156.
- (33) Xu, D. H.; Lohwongwatana, B.; Duan, G.; Johnson, W. L.; Garland, C. *Acta Mater.* **2004**, *52*, 2621–2624.
- (34) Dai, X. D.; Li, J. H.; Liu, B. X. *Appl. Phys. Lett.* **2007**, *90*, 131904.
- (35) Li, J. H.; Dai, Y.; Dai, X. D.; Wang, T. L.; Liu, B. X. *Comput. Mater. Sci.* **2008**, *43*, 1207–1215.
- (36) Yashiro, K.; Nishimura, M.; Tomita, Y. *Model. Simul. Mater. Sci. Eng.* **2006**, *14*, 597–605.
- (37) Li, J. H.; Dai, Y.; Cui, Y. Y.; Liu, B. X. *Mater. Sci. Eng., R* **2011**, *72*, 1–28.
- (38) Cheng, Y. Q.; Ma, E.; Sheng, H. W. *Phys. Rev. Lett.* **2009**, *102*, 245501.